Nonlinear Dynamics **9:** 391–417, 1996.

A Simple Feedback Control System: Bifurcations of Periodic Orbits and Chaos

K. YAGASAKI*
Department of Mechanical Engineering, Tamagawa University, Machida, Tokyo 194, Japan

(Received: 24 March 1994; accepted: 23 March 1995)

Abstract. We consider a pendulum subjected to linear feedback control with periodic desired motions. The pendulum is assumed to be driven by a servo-motor with small time constant, so that the feedback control system can be approximated by a periodically forced oscillator. It was previously shown by Melnikov's method that transverse homoclinic and heteroclinic orbits exist and chaos may occur in certain parameter regions. Here we study local bifurcations of harmonics and subharmonics using the second-order averaging method and Melnikov's method. The Melnikov analysis was performed by numerically computing the Melnikov functions. Numerical simulations and experimental measurements are also given and are compared with the previous and present theoretical predictions. Sustained chaotic motions which result from homoclinic and heteroclinic tangles for not only single but also multiple hyperbolic periodic orbits are observed. Fairly good agreement is found between numerical simulation and experimental results.

Key words: Bifurcation, chaos, pendulum, feedback control, second-order averaging, Melnikov method, experiment.

1. Introduction

In this paper we consider a pendulum subjected to linear feedback control with periodic desired motions. The pendulum is assumed to be driven by a servo-motor with small time constant, so that the feedback control system can be approximated by a periodically forced oscillator. In an earlier paper [1] we showed that chaotic motions may exist for certain parameter regions using Melnikov's method [2, 3]. The chaotic motions result from transverse intersection between the stable and unstable manifolds of not only single but also multiple hyperbolic periodic orbits. Here we study bifurcations of harmonics and second-order subharmonics using the second-order averaging method and Melnikov's method. Numerical simulations and experimental measurements are also given and compared with the previous and present theoretical predictions for periodic and chaotic motions.

Second-order averaging and Melnikov analyses for a large class of periodically forced oscillators were performed in [4]. The second-order averaging analysis suggests that there exist common structures of bifurcation sets near the primary, subharmonic and superharmonic resonances in different systems. We will see that this conjecture is true in our case.

Chaotic motions resulting from homoclinic and heteroclinic tangles for multiple hyperbolic periodic orbits were also experimentally studied by Li and Moon [5]. They used a magnetically buckled beam to demonstrate the existence of chaos in a periodically forced single-degree-of-freedom system with three-well potential. However, in some respects, their experimental observations were considerably different from numerical simulation results for the single-degree-of-freedom model, perhaps mainly because of vibrations in higher modes of the beam.

* Present address: Department of Mechanical Engineering, Gifu University, Gifu, Gifu 501-11, Japan.

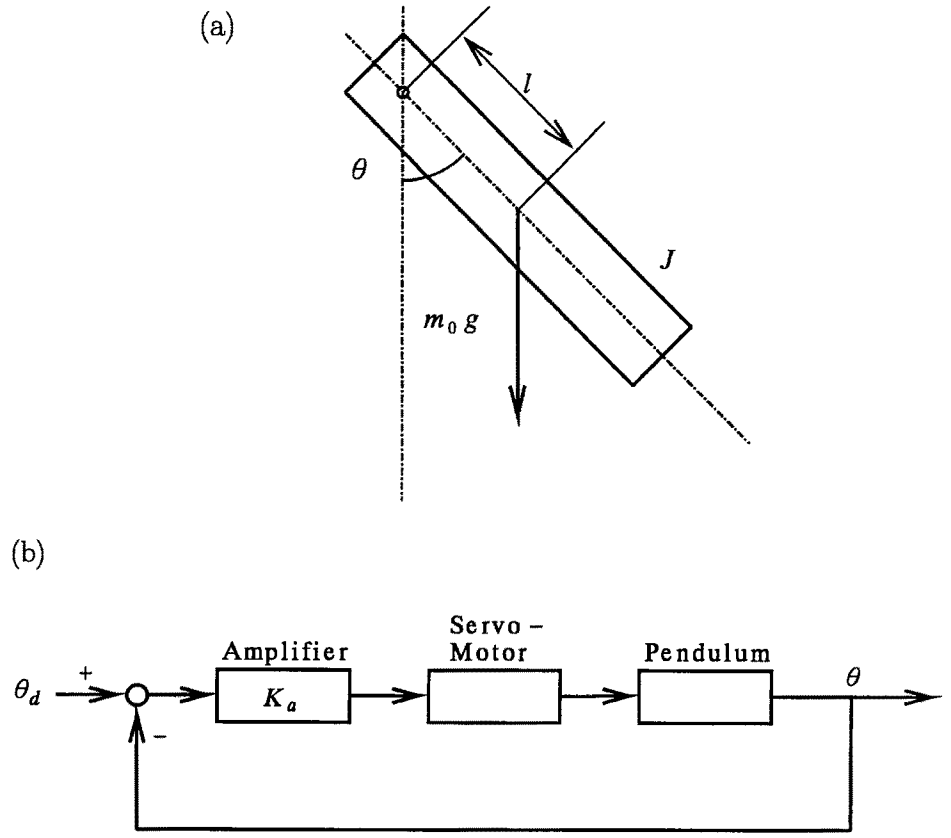

Figure 1. The feedback system. (a) The pendulum; (b) the block diagram.

In our model, we will find a good agreement between numerical simulations and experimental measurements in strange attractors, power spectra of chaotic orbits and parameter regions for the existence of sustained chaos.

This paper is organized as follows. Theoretical results for bifurcations of harmonics and subharmonics are given in Section 2. The second-order averaging analysis for the primary and subharmonic resonances is briefly reviewed. Melnikov's method for subharmonics is then applied and the Melnikov functions are numerically computed. Numerical simulation and experimental results are given in Sections 3 and 4, respectively. Bifurcation sets for harmonics and second-order subharmonics and parameter regions for the existence of steady state chaos are obtained and compared with the theoretical predictions. Sustained chaotic motions which result from homoclinic and heteroclinic tangles for not only single but also multiple hyperbolic periodic orbits are observed. In Section 5 we conclude with a summary and some comments.

2. Theory

2.1. Equation of Motion

We consider a feedback control system in Figure 1. A physical pendulum with mass m_0 and inertial moment J is driven by a servo-motor with resistance R, inductance L, back-electromotive constant K_0, torque constant K_T, and negligible inertia. Electromotive force

proportional to the difference between the prescribed motion $\theta_d(t)$ and the pendulum position θ, $K_a(\theta_d(t) - \theta)$, is applied to the servo-motor. We take $\theta_d(t) = a_1 \cos \Omega t + a_0$ so that the pendulum should swing about $\theta = a_0$ with amplitude a_1 and angular frequency Ω. The pendulum is also assumed to be subjected to damping force proportional to the velocity, $D\dot{\theta}$, resulting from servo-motor friction and so on.

Let ω_n be the natural frequency of the pendulum, i.e., $\omega_n = \sqrt{m_0 g l / J}$ with g the gravitational acceleration and l the distance between the rotational axis and the center of gravity of the pendulum. We assume that the time constant L/R of the servo-motor is much smaller than the period $2\pi/\omega_n$ for small oscillations of the pendulum, i.e., $\omega_n L/R \ll 1$. Change time variable $t \to \omega_n t$ and let $x = \theta$ and $y = \dot{\theta}$. Then the pendulum motion is approximately governed by

$$\begin{aligned} \dot{x} &= y, \\ \dot{y} &= -\sin x - \alpha x + \beta - \bar{\delta} y + \bar{\gamma} \cos \omega t, \end{aligned} \tag{1}$$

where

$$\alpha = \frac{K_T K_a}{m_0 g l R}, \quad \omega = \frac{\Omega}{\omega_n}, \quad \beta = \alpha a_0, \quad \bar{\gamma} = \alpha a_1, \quad \bar{\delta} = \frac{D}{\omega_n J} + \frac{\omega_n K_T K_0}{m_0 g l R}. \tag{2}$$

See [1] for derivation of equation (1).

When $\bar{\delta} = \bar{\gamma} = 0$, equation (1) becomes

$$\begin{aligned} \dot{x} &= y, \\ \dot{y} &= -\sin x - \alpha x + \beta. \end{aligned} \tag{3}$$

Equation (3) corresponds to the non-damping, constant input case and is a Hamiltonian system with a Hamiltonian function

$$H(x, y) = \frac{1}{2} y^2 - \cos x + \frac{1}{2} \alpha x^2 - \beta x. \tag{4}$$

The phase space of equation (3) is shown in Figure 2 for two pairs of α and β. There are centers and saddles with homoclinic orbits. Inside and outside the homoclinic loops there exist one-parameter families of periodic orbits. For some parameter values equation (3) also has heteroclinic orbits. The phase space of equation (3) thus has a great variety depending on the values of α and β. See [1] for the details.

A large class of nonlinear oscillators containing equation (1) were studied in [4]. The second-order averaging and Melnikov methods were used there to describe saddle-node, period-doubling, homoclinic and heteroclinic bifurcations and the results of the second-order averaging and Melnikov analyses for saddle-node bifurcations were compared. In the following we give some results of [4] in the context of equation (1).

2.2. Second-Order Averaging Analysis

Let $(x_0, 0)$ be a center of equation (3), i.e.,

$$-\sin x - \alpha x + \beta = 0, \quad \cos x_0 + \alpha > 0. \tag{5}$$

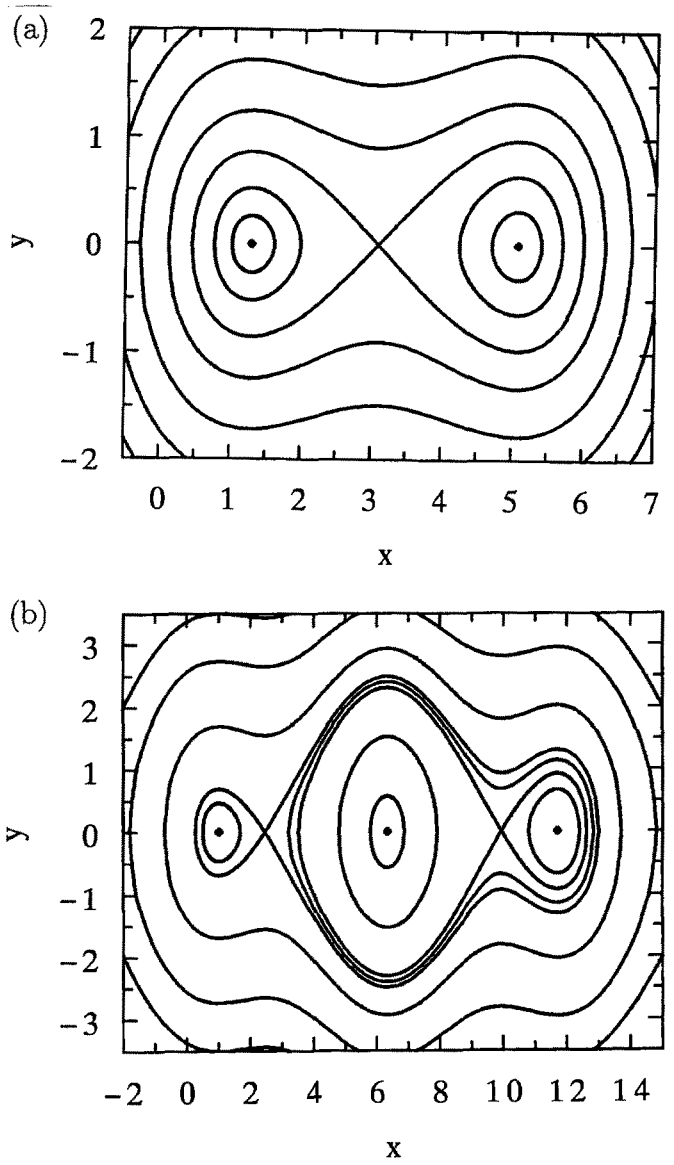

Figure 2. Phase planes of the unperturbed system (3). (a) $\alpha = 0.5$ and $\beta = 1.6$; (b) $\alpha = 0.15$ and $\beta = 1$.

The frequencies of periodic orbits near the center are approximately given by

$$\omega_0 = \sqrt{\cos x_0 + \alpha}.$$

If the ratio of ω to ω_0 is close to a rational number, then resonance behavior may occur in equation (1). Here the results of the second-order averaging analysis for the primary and second-order subharmonic resonances in equation (1) are briefly reviewed. See [4] for details and other resonance behavior in more general systems.

We begin with the case of primary resonance $\omega \approx \omega_0$. Introduce a small parameter ϵ such that $0 < \epsilon \ll 1$ and replace $\bar{\delta}$ and $\bar{\gamma}$ by $\epsilon\delta$ and $\epsilon^{3/2}\gamma$, respectively. We assume that $\omega^2 - \omega_0^2 = O(\epsilon)$ and set $\epsilon\Omega = \omega^2 - \omega_0^2$. Let

$$a_1 = \cos x_0 + \alpha, \quad a_2 = -\frac{1}{2}\sin x_0, \quad a_3 = -\frac{1}{6}\cos x_0, \tag{6}$$

and let $x = x_0 + \sqrt{\epsilon}z$. Then equation (1) can be rewritten as

$$\ddot{z} + \omega_0^2 z = -\sqrt{\epsilon}a_2 z^2 + \epsilon[\gamma\cos\omega t - a_3 z^3 - \delta\dot{z}] + O(\epsilon^{3/2}). \tag{7}$$

We use the van der Pol transformation

$$\begin{pmatrix} u \\ v \end{pmatrix} = \begin{pmatrix} \cos\omega t & -\dfrac{1}{\omega}\sin\omega t \\ -\sin\omega t & -\dfrac{1}{\omega}\omega\cos\omega t \end{pmatrix} \begin{pmatrix} z \\ \dot{z} \end{pmatrix}, \tag{8}$$

and carry out averaging up to second order, so that equation (7) becomes

$$\begin{aligned} \dot{u} &= \frac{\epsilon}{2\omega_0}[-\delta\omega_0 u + \Omega v - b_0(u^2+v^2)v], \\ \dot{v} &= \frac{\epsilon}{2\omega_0}[-\Omega u - \delta\omega_0 v + b_0(u^2+v^2)u - \gamma], \end{aligned} \tag{9}$$

where

$$b_0 = \frac{9a_1a_3 - 10a_2^2}{12a_1} = -\frac{3\alpha\cos x_0 + 2\sin^2 x_0 + 3}{24(\cos x_0 + \alpha)}. \tag{10}$$

Note that $b_0 < 0$ for $0 < \alpha < 1$. Analyzing fixed points of equation (9), which correspond to harmonics of equation (7) and hence equation (1), we can show supercritical saddle-node bifurcations of harmonics occur near the curve

$$\gamma^2 = \frac{2\Omega(\Omega^2 + 9\delta^2\omega_0^2) - 2(\Omega^2 - 3\delta^2\omega_0^2)\sqrt{\Omega^2 - 3\delta^2\omega_0^2}}{27b_0} \tag{11}$$

and subcritical saddle-node bifurcations near the curve

$$\gamma^2 = \frac{2\Omega(\Omega^2 + 9\delta^2\omega_0^2) + 2(\Omega^2 - 3\delta^2\omega_0^2)\sqrt{\Omega^2 - 3\delta^2\omega_0^2}}{27b_0} \tag{12}$$

in the parameter space (Ω, γ). The two curves (11) and (12) meet at

$$(\Omega, \gamma) = \left(-\sqrt{3}\delta\omega_0, \sqrt{8\sqrt{3}(\delta\omega_0)^3/9|b_0|}\right)$$

Below the curve (11) there exists a stable harmonic orbit. Two harmonics appear on the curve (11), and one of them is stable and the other unstable above the curve (11). The unstable harmonic and one of the two stable harmonics disappear on the curve (12) and the other stable harmonic still exists above the curve (12).

We turn to the case of second-order subharmonic resonance $\omega \approx 2\omega_0$ and set $\epsilon\Omega = (\omega^2 - 4\omega_0^2)/4$. Replace $\bar{\delta}$ and $\bar{\gamma}$ by $\epsilon\delta$ and $\epsilon\gamma$ $(0 < \epsilon \ll 1)$, respectively. Letting

$$x = x_0 + \sqrt{\epsilon}z - \epsilon\Gamma\cos\omega t, \tag{13}$$

where $\Gamma = \gamma/3a_1$, we can rewrite equation (1) as

$$\ddot{z} + \omega_0^2 z = -\sqrt{\epsilon}a_2 z^2 + \epsilon[2a_2\Gamma z\cos\omega t - a_3 z^3 - \delta\dot{z}] + O(\epsilon^{3/2}). \tag{14}$$

Again, we use the van der Pol transformation

$$\begin{pmatrix} u \\ v \end{pmatrix} = \begin{pmatrix} \cos\dfrac{\omega t}{2} & -\dfrac{2}{\omega}\sin\dfrac{\omega t}{2} \\ -\sin\dfrac{\omega t}{2} & -\dfrac{2}{\omega}\cos\dfrac{\omega t}{2} \end{pmatrix} \begin{pmatrix} z \\ \dot{z} \end{pmatrix}, \tag{15}$$

and carry out averaging up to second order, so that equation (14) becomes

$$\begin{aligned} \dot{u} &= \frac{\epsilon}{2\omega_0}[-\delta\omega_0 u + (\Omega - a_2\Gamma)v - b_0(u^2+v^2)v], \\ \dot{v} &= \frac{\epsilon}{2\omega_0}[(-\Omega - a_2\Gamma)u - \delta\omega_0 v + b_0(u^2+v^2)u]. \end{aligned} \tag{16}$$

Analyzing fixed points of equation (16), which correspond to harmonics or second-order subharmonics of equation (14) and hence equation (1), we can show that in the (Ω, γ)-space supercritical saddle-node bifurcations of second-order subharmonics occur near the curve

$$\gamma^2 = \frac{9a_1^2}{a_2^2}\,\delta^2\omega_0^2, \quad \Omega < 0, \tag{17}$$

and period-doubling bifurcations of harmonics occur near the curve

$$\gamma^2 = \frac{9a_1^2}{a_2^2}\,(\Omega^2 + \delta^2\omega_0^2), \tag{18}$$

which are supercritical if $\Omega > 0$ and subcritical if $\Omega < 0$.

When $\Omega < 0$, i.e., $\omega < 2\omega_0$, there exists a stable harmonic orbit below the curve (17), and stable and unstable second-order subharmonics appear at a supercritical saddle-node bifurcation on the curve (17). Moreover, the harmonic becomes unstable and the unstable subharmonic disappears at a subcritical period-doubling bifurcation on the curve (18). For $\Omega > 0$, i.e., $\omega > 2\omega_0$, there exists a stable harmonic below the curve (18), the harmonic becomes unstable and a stable second-order subharmonic appears at a supercritical period-doubling bifurcation on the curve (18). In both cases a stable second-order subharmonic continues to exist above the curve (18).

2.3. Melnikov Analysis

In [1] homoclinic and heteroclinic bifurcations in equation (1) were discussed using Melnikov's method. So we give the Melnikov analysis for saddle-node bifurcations of subharmonics in equation (1) here. See also [2, 3] for general information on Melnikov's method.

Consider a one-parameter family of periodic orbits, $\boldsymbol{q}^\kappa(t) = (x^\kappa(t), y^\kappa(t))$ with $\kappa \in (\kappa_1, \kappa_2)$, where κ_1 and κ_2 are constants. Let $\boldsymbol{q}^\kappa(t)$ be a periodic orbit of period $2\pi m/n\omega$ with m and n relatively prime. The Melnikov function for $\boldsymbol{q}^\kappa(t)$ is given by

$$M^{m/n}(t_0) = \int_0^{2\pi m/\omega} y^\kappa(t)[-\delta y^\kappa(t) + \gamma\cos\omega(t+t_0)]\,\mathrm{d}t$$

$$= \gamma[C^{m/n}(\alpha,\beta,\omega)\cos\omega t_0 - S^{m/n}(\alpha,\beta,\omega)\sin\omega t_0] - \delta B^{m/n}(\alpha,\beta,\omega)$$
$$= \gamma A^{m/n}(\alpha,\beta,\omega)\cos[\omega t_0 + \Theta^{m/n}(\omega)] - \delta B^{m/n}(\alpha,\beta,\omega), \tag{19}$$

where

$$C^{m/n}(\alpha,\beta,\omega) = \int_0^{2\pi m/\omega} y^\kappa(t)\cos\omega t\,\mathrm{d}t,$$
$$S^{m/n}(\alpha,\beta,\omega) = \int_0^{2\pi m/\omega} y^\kappa(t)\sin\omega t\,\mathrm{d}t,$$
$$B^{m/n}(\alpha,\beta,\omega) = \int_0^{2\pi m/\omega} [y^\kappa(t)]^2\,\mathrm{d}t > 0,$$
$$A^{m/n}(\alpha,\beta,\omega) = \sqrt{[C^{m/n}(\alpha,\beta,\omega)]^2 + [S^{m/n}(\alpha,\beta,\omega)]^2},$$
$$\Theta^{m/n}(\alpha,\beta,\omega) = \arctan\left(\frac{S^{m/n}(\alpha,\beta,\omega)}{C^{m/n}(\alpha,\beta,\omega)}\right). \tag{20}$$

Note that $B^{m/n}$ also depend on ω as well as $C^{m/n}$ and $S^{m/n}$. We can show that $M^{m/n}(t_0)$ can have simple zeros only if $n = 1$ (see [4]).

We assume that $n = 1$ and set $M^m(t_0) = M^{m/1}(t_0)$, $A^m(\alpha,\beta,\omega) = A^{m/1}(\alpha,\beta,\omega)$ and $B^m(\alpha,\beta,\omega) = B^{m/1}(\alpha,\beta,\omega)$. If $\gamma/\delta > B^m(\alpha,\beta,\omega)/A^m(\alpha,\beta,\omega) \equiv R^m(\alpha,\beta,\omega)$, then $M^m(t_0)$ has simple zeros and there exist subharmonics of period $2\pi m/\omega$. Moreover, a supercritical saddle-node bifurcation at which a pair of m-th order subharmonics are created occurs at

$$\gamma/\delta = R^m(\alpha,\beta,\omega) + O(\epsilon). \tag{21}$$

2.4. Numerical Computation of the Melnikov Functions

Equation (21) represents approximate saddle-node bifurcation sets for subharmonics in equation (1). However, it is difficult to obtain analytical expressions for the periodic orbits in the unperturbed system (3), and so numerical computations of the integrals in equation (20) are required. In [1] such an approach was performed for the homoclinic bifurcation case using the method proposed by Bruhn and Koch [6]. We now extend their method to the saddle-node bifurcation case.

Let H^κ be the Hamiltonian energy for $\boldsymbol{q}^\kappa(t)$. We assume that $y^\kappa(0) = 0$ and $y^\kappa(t) > 0$ for $0 < t < T^\kappa/2$, where T^κ is the period of $\boldsymbol{q}^\kappa(t)$. From equation (4) we have

$$\frac{\mathrm{d}x}{\mathrm{d}t} = \sqrt{2H^\kappa + 2\cos x - \alpha x^2 + 2\beta x}, \tag{22}$$

on $\boldsymbol{q}^\kappa(t)$ for $0 < t < T^\kappa/2$. Let $(x_1, 0)$ and $(x_2, 0)$ $(x_1 < x_2)$ be two points at which $\boldsymbol{q}^\kappa(t)$ crosses the x-axis in the phase plane (cf. Figure 3). Then $x^\kappa(0) = x_1$, $x^\kappa(T^\kappa/2) = x_2$ and $y^\kappa(t)$ is an odd function of t. Rearranging equation (22) and integrating it, we obtain

$$t = \int_{x_1}^{x} \frac{\mathrm{d}\xi}{\sqrt{2H^\kappa + 2\cos\xi - \alpha\xi^2 + 2\beta\xi}} \tag{23}$$

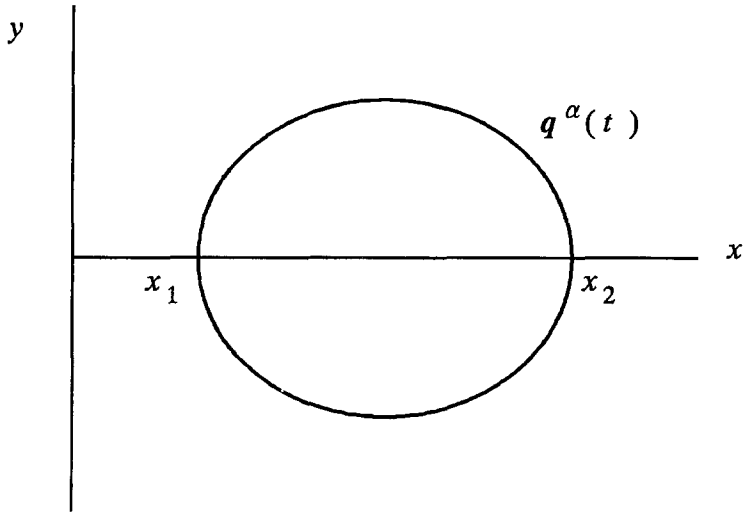

Figure 3. A periodic orbit.

for $0 < t < T^{\kappa}/2$. Hence,

$$T^{\kappa} = 2\int_{x_1}^{x_2} \frac{\mathrm{d}x}{\sqrt{2H^{\kappa} + 2\cos x - \alpha x^2 + 2\beta x}}. \tag{24}$$

By the resonance relationship, we also have

$$T^{\kappa} = \frac{2\pi m}{\omega} \tag{25}$$

Substituting equations (22) and (23) into the third and fourth equations of (20) and using the fact that $y^{\kappa}(t)$ is odd, we obtain

$$\begin{aligned} A^m(\alpha,\beta,\omega) &= 2\left|\int_{x_1}^{x_2} \sin\left(\omega\int_{x_1}^{x} \frac{\mathrm{d}\xi}{\sqrt{2H^{\kappa} + 2\cos\xi - \alpha\xi^2 + 2\beta\xi}}\right)\mathrm{d}x\right|, \\ B^m(\alpha,\beta,\omega) &= 2\int_{x_1}^{x_2} \sqrt{2H^{\kappa} + 2\cos x - \alpha x^2 + 2\beta x}\ \mathrm{d}x. \end{aligned} \tag{26}$$

We can numerically estimate condition (21) for a periodic orbit $q^{\kappa}(t)$ passing through $(x_1, 0)$ as follows.

(a) x_1 and m are given.

(b) Compute $H^{\kappa} = -\cos x_1 + \frac{1}{2}\alpha x_1^2 - \beta x_1$.

(c) Numerically solve the transcendent equation

$$-2\cos x + \alpha x^2 - 2\beta x = 2H^{\kappa} \tag{27}$$

to obtain x_2 ($> x_1$).

(d) Numerically integrate equation (24) to obtain T^{κ}.

(e) Obtain ω from equation (25).

(f) Carry out the integrations in equation (26) numerically to obtain $A^m(\alpha,\beta,\omega)$ and $B^m(\alpha,\beta,\omega)$.

(g) Compute condition (21).

The integration of $A^m(\alpha, \beta, \omega)$ is performed by changing the lower and upper limits of integration from x_1 and x_2 to $x_1 + \Delta x$ and $x_2 - \Delta x$, respectively, where Δx is a small positive constant since the integrand is singular near these point.

2.5. Numerical Examples

We give numerical examples for the following two cases:
(i) $\alpha = 0.5$ and $\beta = 1.6$,
(ii) $\alpha = 0.15$ and $\beta = 1$.
The damping constant was fixed as $\bar{\delta} = 0.12$ while the input amplitude $\bar{\gamma}$ and the frequency ω were varied. The unperturbed system (3) has one saddle and two centers for case (i); and two saddles and three centers for cases (ii). See Figure 2 for the phase space of the unperturbed system (3) with these parameter values. For these two cases, homoclinic bifurcation sets given by Melnikov's method were obtained and the stable and unstable manifolds of hyperbolic periodic orbits were numerically computed to verify the theoretical results in [1].

Figure 4 shows the saddle-node and homoclinic bifurcation sets for case (i). The bifurcation sets near the primary resonance are depicted in Figure 4(a), and the bifurcation sets near the second-order subharmonic resonance in Figure 4(b). The dotted and broken curves represent the bifurcation sets given by the second-order averaging analysis for harmonics or second-order subharmonics near the left and right unperturbed centers, respectively, while the dashed-and-dotted curve represents the saddle-node bifurcation set given by the Melnikov analysis for harmonics outside the unperturbed homoclinic loops. Supercritical and subcritical saddle-node bifurcations of harmonics or subharmonics are denoted by *sn* and *sn'*, respectively, and supercritical and subcritical period-doubling bifurcations of harmonics by *pd* and *pd'*, respectively. The solid curves with R_1^- and R_1^+, respectively, represent the homoclinic bifurcation sets obtained by Melnikov's method for the left and right homoclinic loops [1]. Above these curves the stable and unstable manifolds of a hyperbolic periodic orbit near the unperturbed saddle intersect transversely. Saddle-node bifurcation sets obtained by Melnikov's method for harmonics and subharmonics inside the homoclinic loops are not given since the Melnikov analysis gives less information than the second-order averaging analysis on these bifurcation sets near the primary and second-order subharmonic resonances (see [4]). We see that the saddle-node bifurcation curve for harmonics outside the homoclinic loops has two values of $\bar{\gamma}$, say $\bar{\gamma}_1 < \bar{\gamma}_2$, for some values of ω. This implies that there exist two periodic orbits outside the homoclinic loops for $\bar{\gamma} > \bar{\gamma}_2$ at such values of ω.

Figure 5 shows a similar result near the primary resonance for case (ii). The dotted, broken and dashed curves represent the bifurcation sets given by the second-order averaging analysis for harmonics near the left, middle and right unperturbed centers, respectively, while the dashed-and-dotted and dashed-dotted-and-dotted curves, respectively, represent the saddle-node bifurcation sets given by the Melnikov analysis for harmonics outside the homoclinic loops for the left and right unperturbed saddles. The solid curves with $R_1^{\pm}$ and $R_2^{\pm}$, respectively, represent the homoclinic bifurcation sets obtained by Melnikov's method for the homoclinic orbits of the left and right saddles [1]. The others are the same as in Figure 4.

3. Numerical Simulation

Numerical simulations of equation (1) were performed using the Runge–Kutta–Gill method [7] with 128 steps per period $2\pi/\omega$ of the reference signal. As in Section 2.5, the following

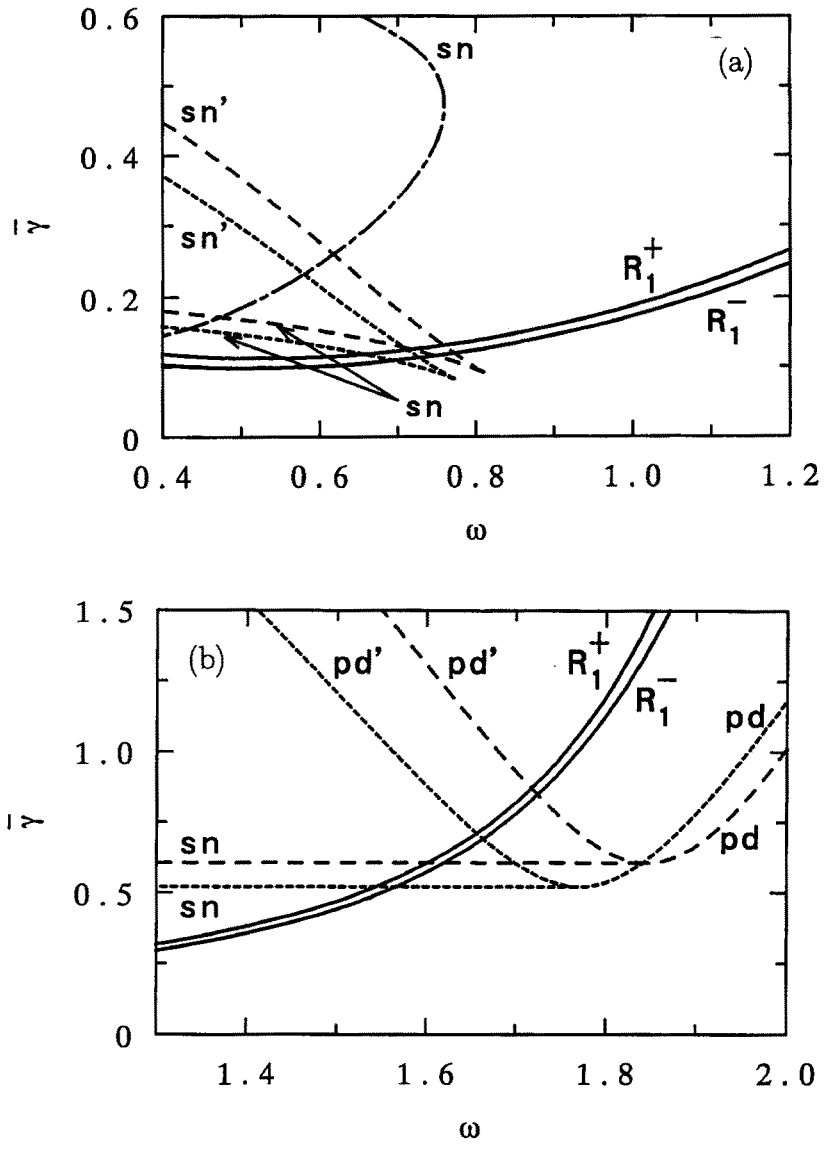

Figure 4. Bifurcation sets given by the second-order averaging and Melnikov analyses in case (i). (a) Near the primary resonance; (b) near the second-order subharmonic resonance.

two cases with $\bar{\delta} = 0.12$ were considered: (i) $\alpha = 0.5$ and $\beta = 1.6$; (ii) $\alpha = 0.15$ and $\beta = 1$. The input amplitude $\bar{\gamma}$ and the frequency ω were varied.

Figure 6 shows a bifurcation diagram for $\omega = 0.75$ in case (i) and Figure 7 several examples of phase plane motions in (x, y). For $\bar{\gamma}$ small, there exists one stable harmonic near each center in the unperturbed system (3) (cf. Figure 7(a)). As $\bar{\gamma}$ increases, the harmonics near the left and right centers disappear in subcritical saddle-node bifurcations at $\bar{\gamma} \approx 0.092$ and $\bar{\gamma} \approx 0.134$, respectively. Other stable harmonics near the left and right centers (cf. Figure 7(b)) appear in supercritical saddle-node bifurcations at $\bar{\gamma} \approx 0.080$ and $\bar{\gamma} \approx 0.096$, respectively. A supercritical period-doubling bifurcation in which the harmonic near the left center becomes unstable and a stable second-order subharmonic (cf. Figure 7(c)) appears occur at $\bar{\gamma} \approx 0.156$.

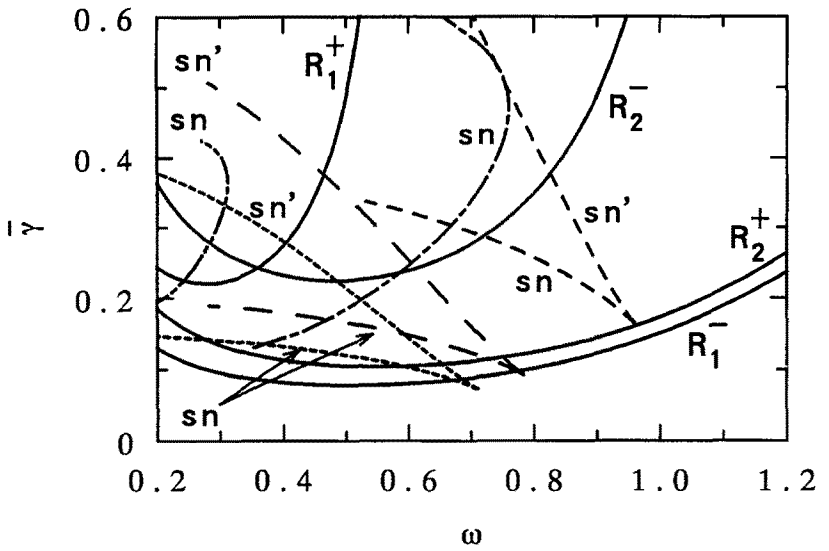

Figure 5. Bifurcation sets given by the second-order averaging and Melnikov analyses near the primary resonance in case (ii).

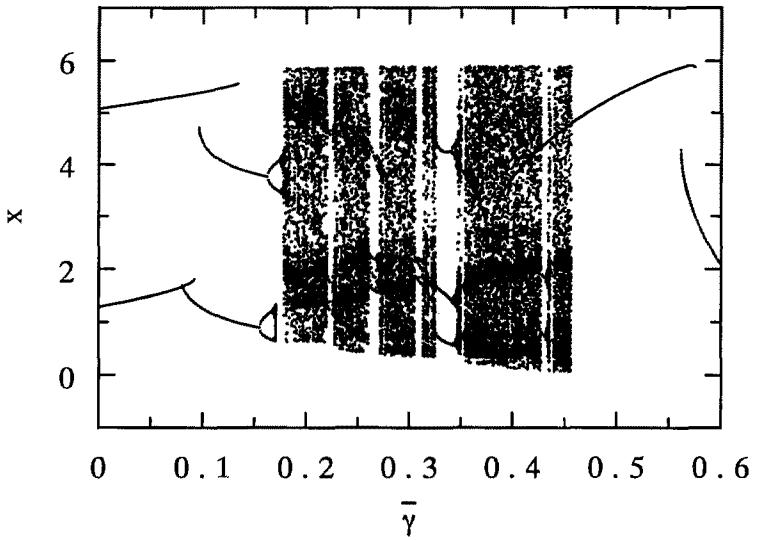

Figure 6. A bifurcation diagram for $\omega = 0.75$ in case (i).

Further period-doubling bifurcations occur and accumulate to chaos at $\bar{\gamma} \approx 0.170$. The chaotic attractor suddenly disappears at $\bar{\gamma} \approx 0.171$. The harmonic near the right center undergoes a period-doubling bifurcation and a stable second-order subharmonic (cf. Figure 7(d)) appears at $\bar{\gamma} \approx 0.164$. A sequence of period-doubling bifurcations also occur and accumulate to chaos at $\bar{\gamma} \approx 0.177$. The size of the chaotic attractor suddenly changes and a chaotic orbit such as shown in Figure 7(e) appears at $\bar{\gamma} \approx 0.180$.

Figure 8 shows an orbit of the Poincaré map and a power spectrum of $x(t)$ for the chaotic attractor. Figure 8(a) was produced by sampling $x(t)$ and $y(t)$ for a numerical solution of (1) when the phase of the input equals zero, i.e., $\omega t = 0 \bmod 2\pi$. To produce Figure 8(b), power spectra for 16 samples of duration $512 \times 2\pi/\omega$, each containing 4096 data points,

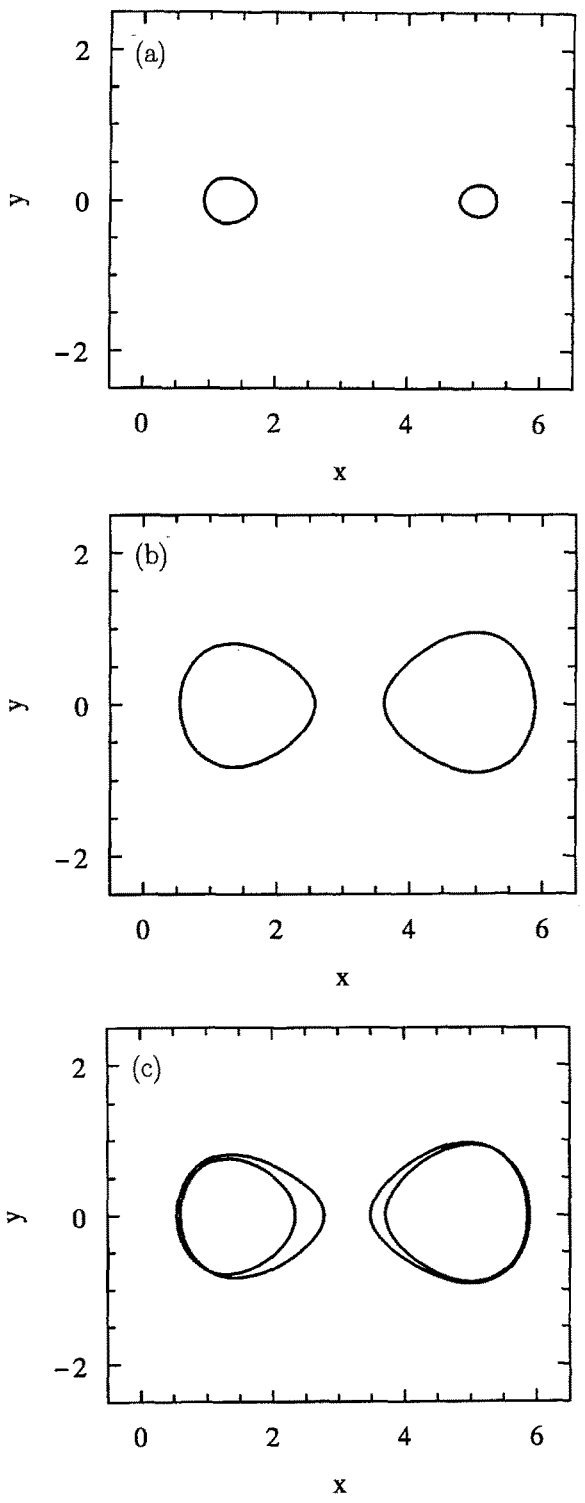

Figure 7(a)–(c).

Figure 7. Phase plane motions in (x, y) for $\omega = 0.75$ in case (i). (a) $\bar{\gamma} = 0.08$; (b) $\bar{\gamma} = 0.15$; (c) $\bar{\gamma} = 0.165$; (d) $\bar{\gamma} = 0.3$; (e) $\bar{\gamma} = 0.57$; (f) $\bar{\gamma} = 0.15$.

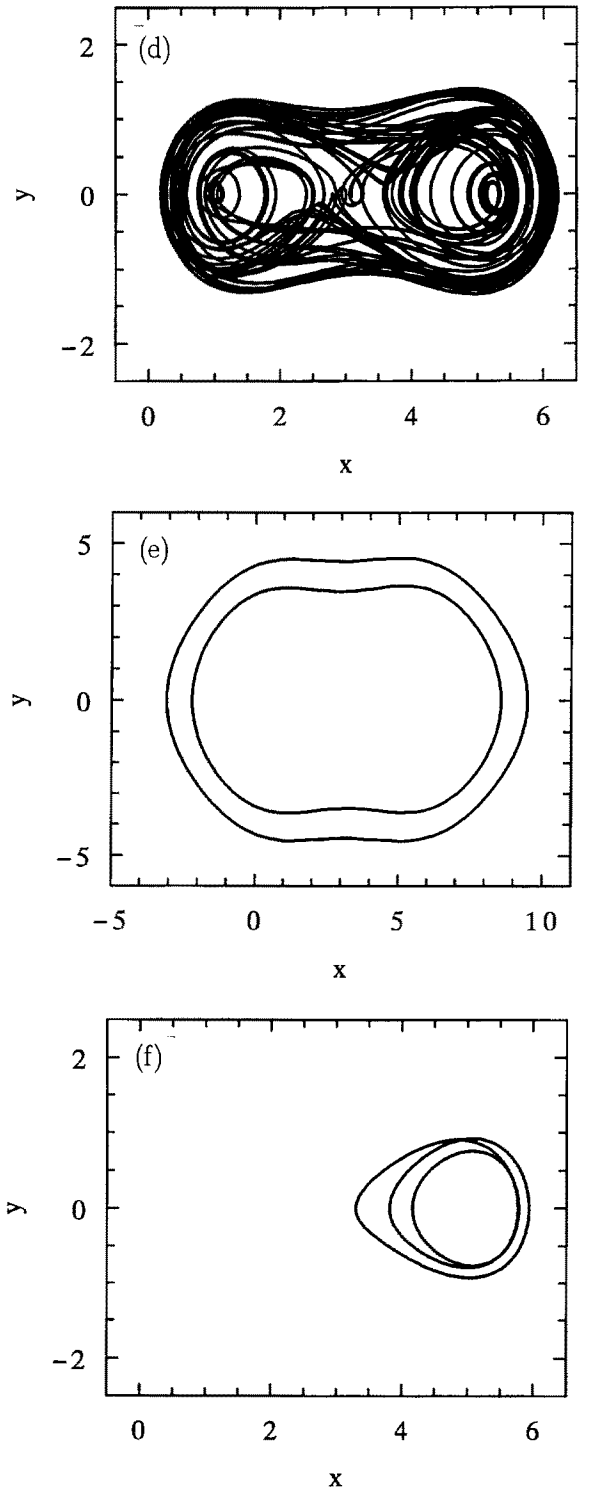

Figure 7(d)–(f).

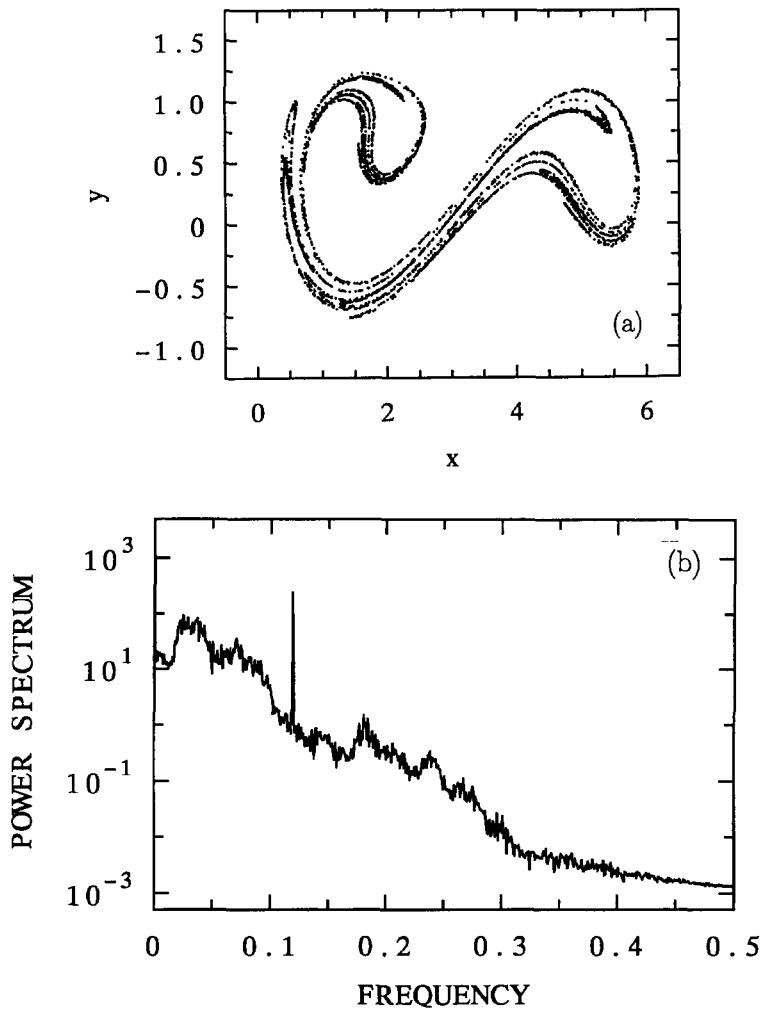

Figure 8. A chaotic motion for $\bar{\gamma} = 0.3$ and $\omega = 0.75$ in case (i). (a) An orbit of the Poincaré map; (b) a power spectrum of $x(t)$.

were obtained by a fast Fourier transform program and then averaged. The strange attractor in Figure 8(a) seems to be the closure of the unstable manifold of a saddle point of the Poincaré map in Figure 10(c) of [1]. The sustained chaotic motion is thus considered to result from homoclinic tangles for single hyperbolic periodic orbit.

As $\bar{\gamma}$ continues to increase, chaotic motions were observed till $\bar{\gamma} \approx 0.456$. They coexist with stable harmonics and subharmonics in some regions while only stable periodic motions were observed in other regions, which correspond to windows of periodic orbits in the bifurcation diagram of Figure 6. For relatively high values of $\bar{\gamma}$ there exist two large stable harmonics (cf. Figure 7(e)) outside the homoclinic loops in the unperturbed system (3). One appears at $\bar{\gamma} \approx 0.378$ and disappears at $\bar{\gamma} \approx 0.575$, and the other appears at $\bar{\gamma} \approx 0.562$.

Figure 9 shows bifurcation sets for harmonics and regions for the existence of sustained chaos near the primary resonance in case (i). The dotted and broken curves represent the bifurcation sets for harmonics near the left and right centers, respectively, while the dashed-

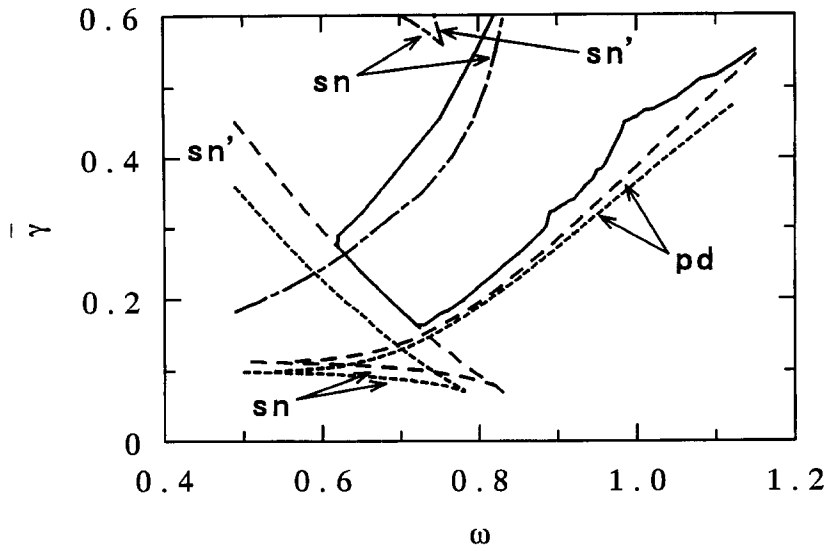

Figure 9. Bifurcation sets for harmonics and regions for the existence of sustained chaos near the primary resonance in case (i).

and-dotted curves represent the bifurcation sets for large harmonics outside the unperturbed homoclinic loops. Supercritical and subcritical saddle-node bifurcations of harmonics are denoted by *sn* and *sn'*, respectively, while supercritical period-doubling bifurcations of harmonics are denoted by *pd*. The solid curves represent the boundaries of a region for sustained chaos. In some parts of the region, which are too complicated to be drawn in Figure 9, only stable periodic motions were observed. Some of these regions correspond to windows of periodic orbits in bifurcation diagrams of Figure 6. Very narrow regions for the existence of sustained chaos are also not drawn in Figure 9. The bifurcation structures near the left and right centers are very similar to those near centers in other forced oscillators with single- and double-well potential [8–12]. The supercritical and subcritical saddle-node bifurcation curves are in good agreement with the theoretical predictions of Figure 4(a) while the theories of Section 2 said nothing about supercritical period-doubling bifurcations of harmonics.

Figure 10 shows a bifurcation diagram for $\omega = 1.75$ in case (i). Again, there exists one stable harmonic near each center in the unperturbed system (3) for $\bar{\gamma}$ small. As $\bar{\gamma}$ increases, the harmonic near the left center becomes unstable and a stable second-order subharmonic appears in a supercritical period-doubling bifurcation at $\bar{\gamma} \approx 0.506$. The harmonic near the right center suddenly disappears at $\bar{\gamma} \approx 0.592$. This implies that a subcritical period-doubling bifurcation, at which the stable harmonic becomes unstable and an unstable second-order subharmonic disappears, occurs as stated in Section 2.2. A stable second-order subharmonic near the right center appears in a supercritical saddle-node bifurcation at $\bar{\gamma} \approx 0.526$ and undergoes a period-doubling bifurcation at $\bar{\gamma} \approx 1.320$. Further period-doubling bifurcations occur and accumulate to chaos at $\bar{\gamma} \approx 1.470$. The chaotic attractor suddenly disappears at $\bar{\gamma} \approx 1.484$. A stable third-order subharmonic also appears in a saddle-node bifurcation at $\bar{\gamma} \approx 0.871$.

Figure 11 shows bifurcation sets for harmonics and second-order subharmonics and regions for sustained chaos near the second-order subharmonic resonance in case (i). Supercritical saddle-node bifurcations of second-order subharmonics are denoted by *sn*, and supercritical

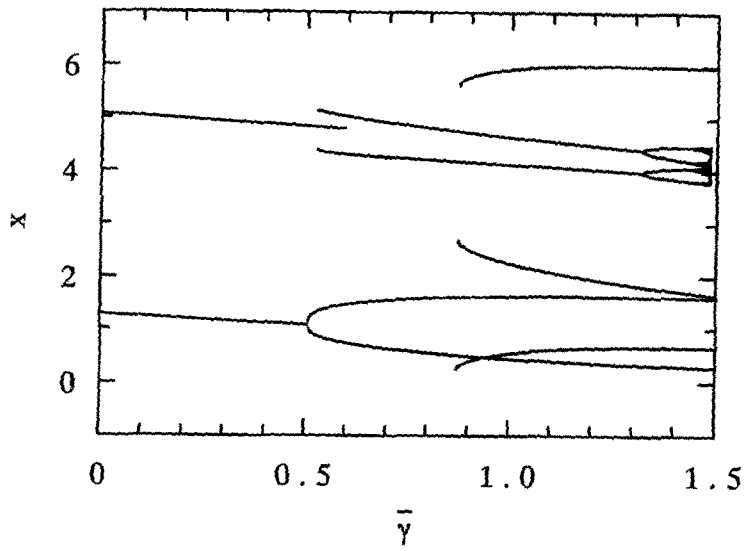

Figure 10. A bifurcation diagram for $\omega = 1.75$ in case (i).

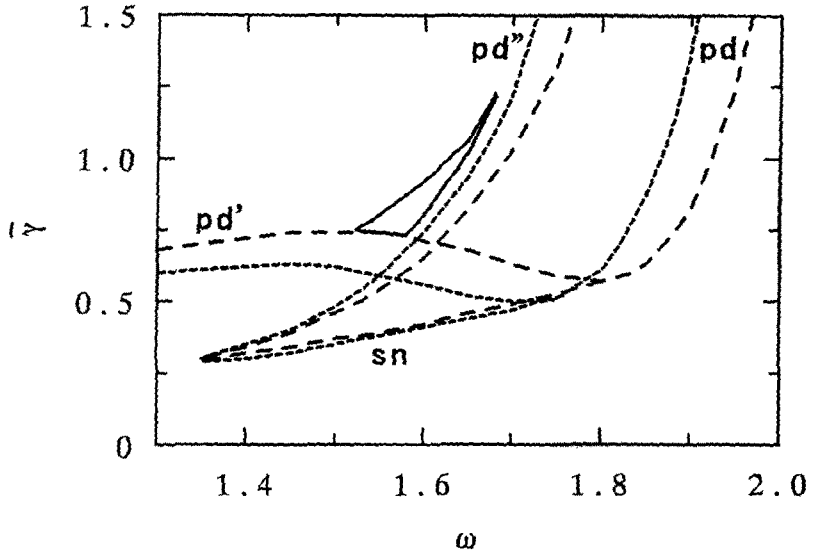

Figure 11. Bifurcation sets for harmonics and subharmonics and regions for the existence of sustained chaos near the second-order subharmonic resonance in case (i).

period-doubling bifurcations of harmonics are denoted by *pd*. The curves labeled *pd'* represent subcritical period-doubling bifurcations of harmonics and the curves labeled *pd"* supercritical period-doubling bifurcations of second-order subharmonics. The others are the same as in Figure 9. Again, very narrow regions for sustained chaos are not drawn in Figure 11. The bifurcation structures near the left and right centers are very similar to those near centers in the Duffing oscillator with double-well potential [12]. The supercritical and subcritical period-doubling bifurcation curves for harmonics and supercritical saddle-node bifurcation curves for second-order subharmonics are qualitatively in good agreement with the theoretical

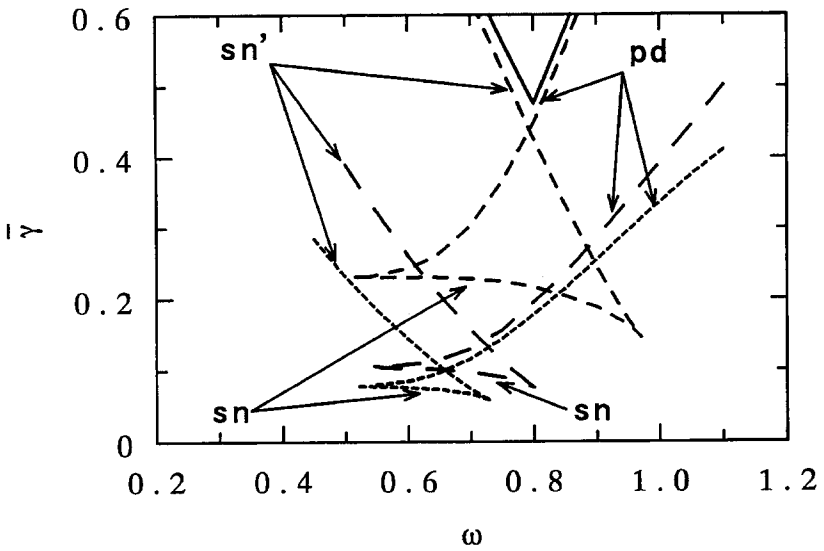

Figure 12. Bifurcation sets for harmonics and regions for the existence of sustained chaos near the primary resonance in case (ii).

predictions of Figure 4(b) although supercritical period-doubling bifurcations of second-order subharmonics were not predicted theoretically in Section 2.

Figure 12 shows bifurcation sets for harmonics and regions for sustained chaos near the primary resonance in case (ii). The dotted, broken and dashed curves represent the bifurcation sets for harmonics near the left, middle and right centers in the unperturbed system (3), respectively. The others are the same as in Figure 9. Figure 13 shows phase plane motions in (x, y). For $\bar{\gamma}$ small, there exists one stable harmonic near each unperturbed center (cf. Figure 13(a)). As in case (i), when $\bar{\gamma}$ increases, saddle-node and period-doubling bifurcations occur near each center and sustained chaotic motions exist for some regions (cf. Figure 13(b)). The bifurcation structures near the three centers are very similar to those near the two centers in case (i) and even to those near centers in other single- and double-well oscillators. The supercritical and subcritical saddle-node bifurcation curves for harmonics near each center are in good agreement with the theoretical predictions of Figure 5. However, large stable harmonics enclosing the homoclinic loops of the left saddle in the unperturbed system (3) (cf. Figure 13(c)) were observed only for much higher values of $\bar{\gamma}$ than the theoretical predictions. Moreover, no stable harmonics enclosing only the homoclinic loops of the right unperturbed saddle was observed.

Figure 14 shows an orbit of the Poincaré map and a power spectrum for the chaotic motion of Figure 13(b). The strange attractor in Figure 14(a) also seems to be the union of closures of the unstable manifolds of two saddle points of the Poincaré map in Figures 11(d) of [1]. The sustained chaotic motion is thus considered to result from homoclinic and heteroclinic tangles for two hyperbolic periodic orbits.

The parameter regions for the existence of sustained chaos are very different from the theoretical predictions by the Melnikov analysis (see Figure 15). This is because Melnikov's method only permits us to predict transverse intersection between the stable and unstable manifolds of hyperbolic periodic orbits, which does not always imply the occurrence of sustained chaos. However, if there are two or more attractors, transverse intersection between

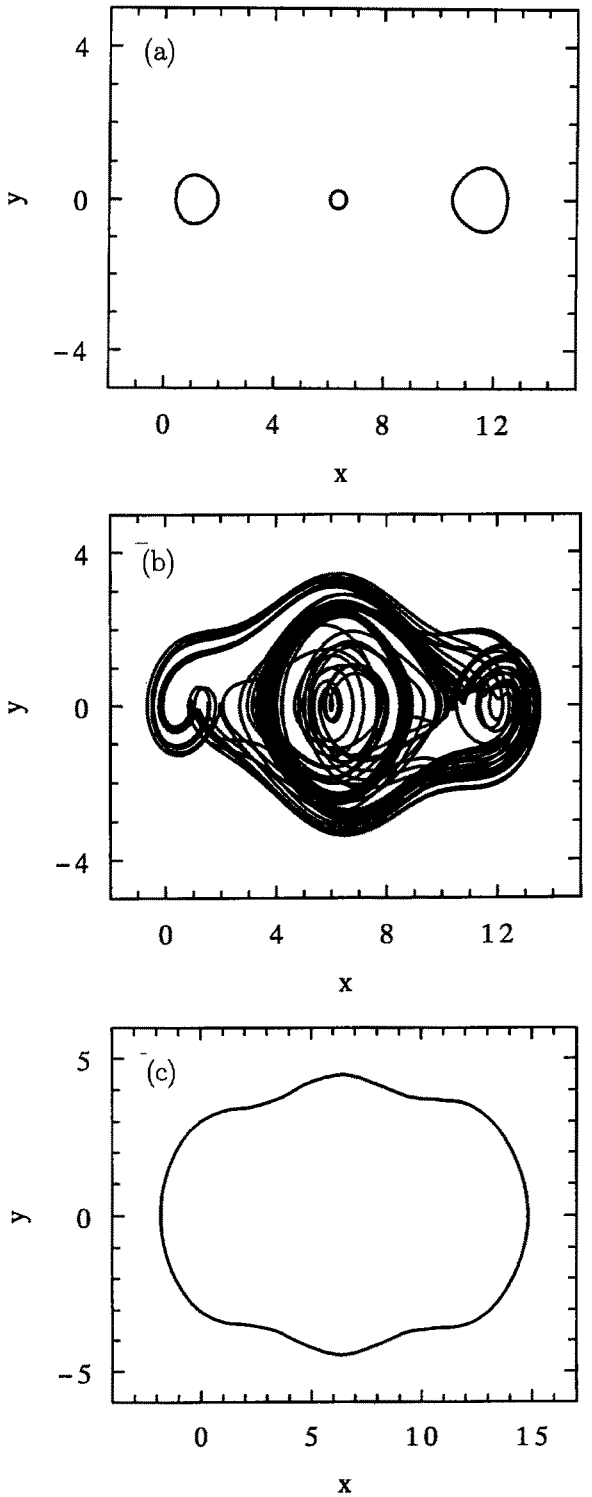

Figure 13. Phase plane motions in (x, y) for case (ii). (a) $\bar{\gamma} = 0.15$ and $\omega = 0.8$; (b) $\bar{\gamma} = 0.7$ and $\omega = 0.8$; (c) $\bar{\gamma} = 0.95$ and $\omega = 0.55$.

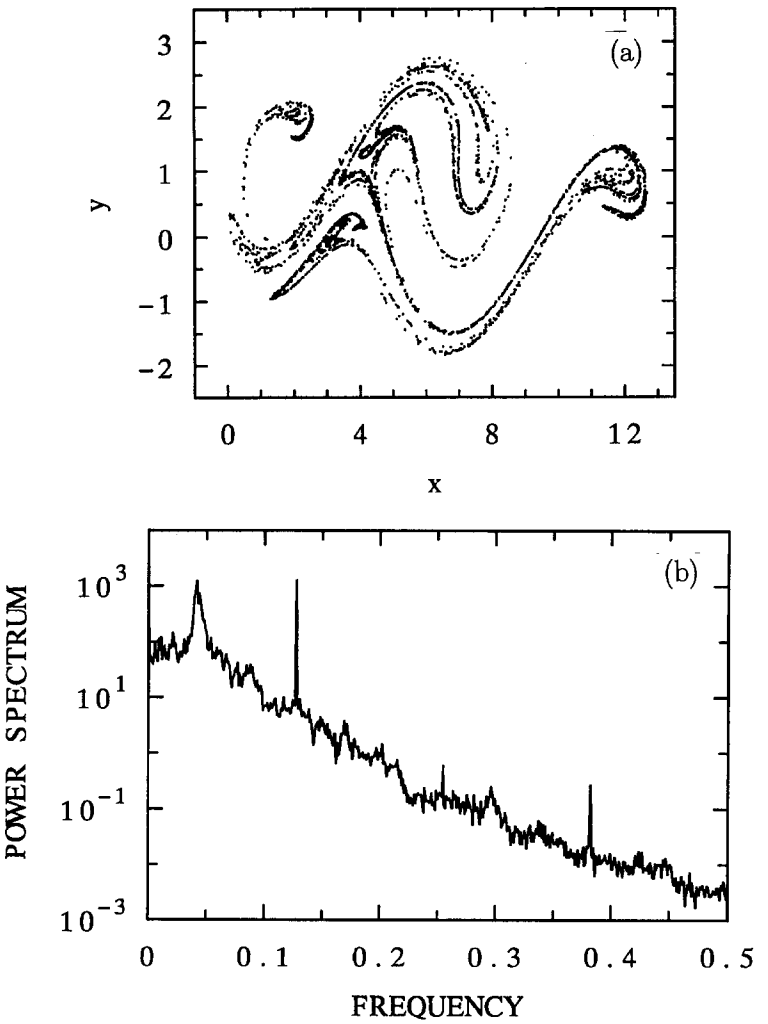

Figure 14. A chaotic motion for $\bar{\gamma} = 0.7$ and $\omega = 0.8$ in case (ii). (a) An orbit of the Poincaré map; (b) a power spectrum of $x(t)$.

the stable and unstable manifolds may yield fractal basin boundaries for the attractors [13]. Figure 16 shows an example of such fractal basin boundaries for $\bar{\gamma} = 0.15$ and $\omega = 0.75$ in case (i). Orbits with black and gray marked initial conditions of (x, y) at $t = 0$ converge to harmonics near the left and right centers shown in Figures 7(b), respectively, while orbits with white marked initial conditions converge to a third-order subharmonic near the right center shown in Figure 7(f).

4. Experiment

4.1. Experimental Model

The experimental apparatus is shown in Figure 17. A pendulum was driven by a servo-motor to which electromotive force proportional to the difference between the desired position $\theta_d(t) = a_1 \cos \Omega t + a_0$ and the pendulum position θ, $K_a(\theta_d(t) - \theta)$, was applied.

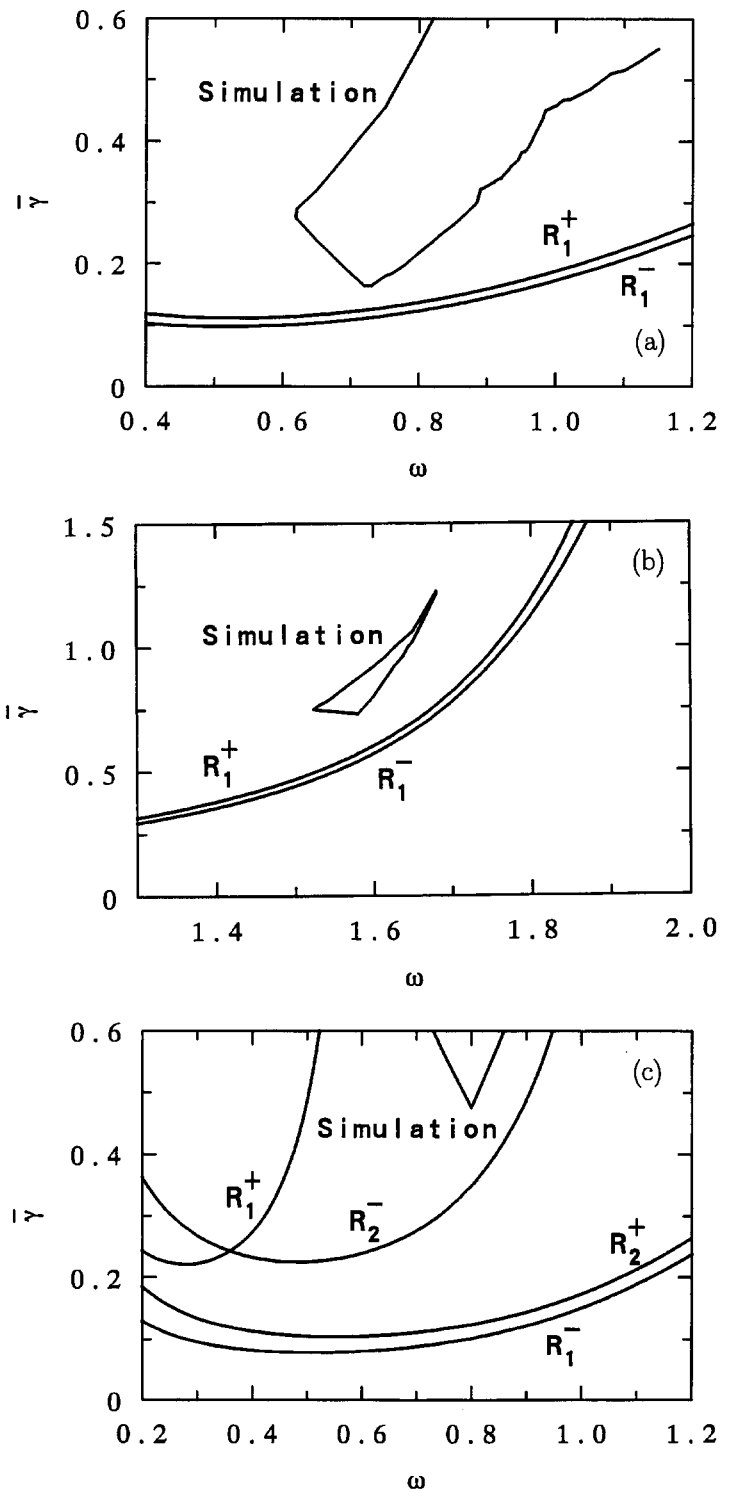

Figure 15. Comparison between the theoretical predictions and numerical simulation results for the existence of chaos (cf. Figures 4 and 5). (a) Near the primary resonance in case (i); (b) near the second-order subharmonic resonance in case (i); (c) near the primary resonance in case (ii). Note that the chaotic motions predicted by the Melnikov theory are not necessarily in steady states.

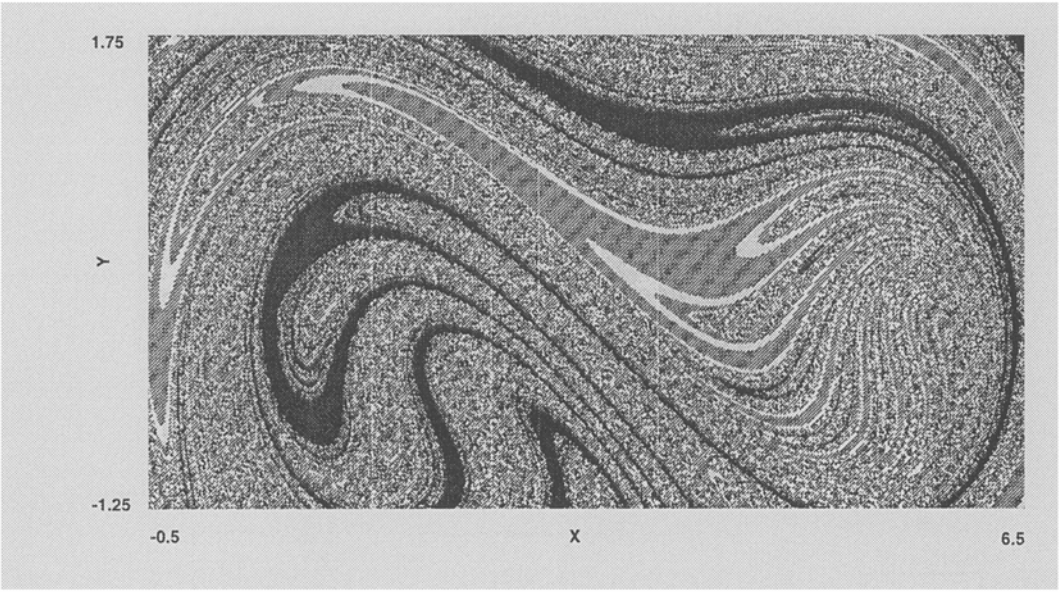

Figure 16. Fractal basin boundaries for $\bar{\gamma} = 0.15$ and $\omega = 0.75$ in case (i). This figure was produced using the software "Dynamics" [14].

As shown in Figure 17(a), the pendulum consists of a brass rod 120(mm) long with a 10(mm) diameter circular cross-section, and a 36(mm) diameter brass disk 16(mm) thick with a 5(mm) diameter hole, which was attached to the shaft of the servo-motor. The mass and inertial moment of the pendulum are $m_0 = 0.22$(kg) and $J = 6.1 \times 10^{-4}$(kgm^2), respectively, and the distance between the rotational axis and the center of gravity of the pendulum is $l = 29$(mm). The natural angular frequency for small oscillations of the pendulum is given by $\omega_n = \sqrt{m_0 g l / J} = 10.1$(rad/s). The pendulum position θ was measured with a potentiometer attached to the shaft of the servo-motor. The output voltage of the potentiometer was $V_b = 1.25$(V) when $\theta = 0$(rad), and the increase of the voltage per unit angular $\Delta V = 0.328$(V/rad).

As shown in Figure 17(b), the output signal of the potentiometer was electronically subtracted from the reference signal produced by a signal generator. The resulting signal was amplified through a power amplifier and then sent to the servo-motor. Letting $V_d(t) = V_1 \cos \Omega t + V_0$ be the reference signal and K the amplification factor of the power amplifier, we have

$$K_a = K\Delta V, \quad a_1 = \frac{V_1}{\Delta V}, \quad a_0 = \frac{V_0 - V_b}{\Delta V}. \tag{28}$$

The nominal resistance and inductance of the servo-motor were 4.9(Ω) (containing the leads) and 1.6(mH) so that $\omega_n L/R \approx 3.3 \times 10^{-3}$. Thus, the time constant of the servo-motor was expected to be much smaller than the natural period of the pendulum.

To measure the velocity of the pendulum the output signal of the potentiometer was differentiated with an electronic differentiation circuit. The displacement and velocity signals were passed through low-pass filters with 50 Hz cut-off frequencies and then fed to a spectrum analyzer, which produced power spectra and stored data at constant or external sampling rates. The Poincaré map was obtained using a pulse synchronous with the reference signal as the sampling trigger signal: the displacement and velocity of the pendulum were displayed at a periodic time interval. See Figure 17(b).

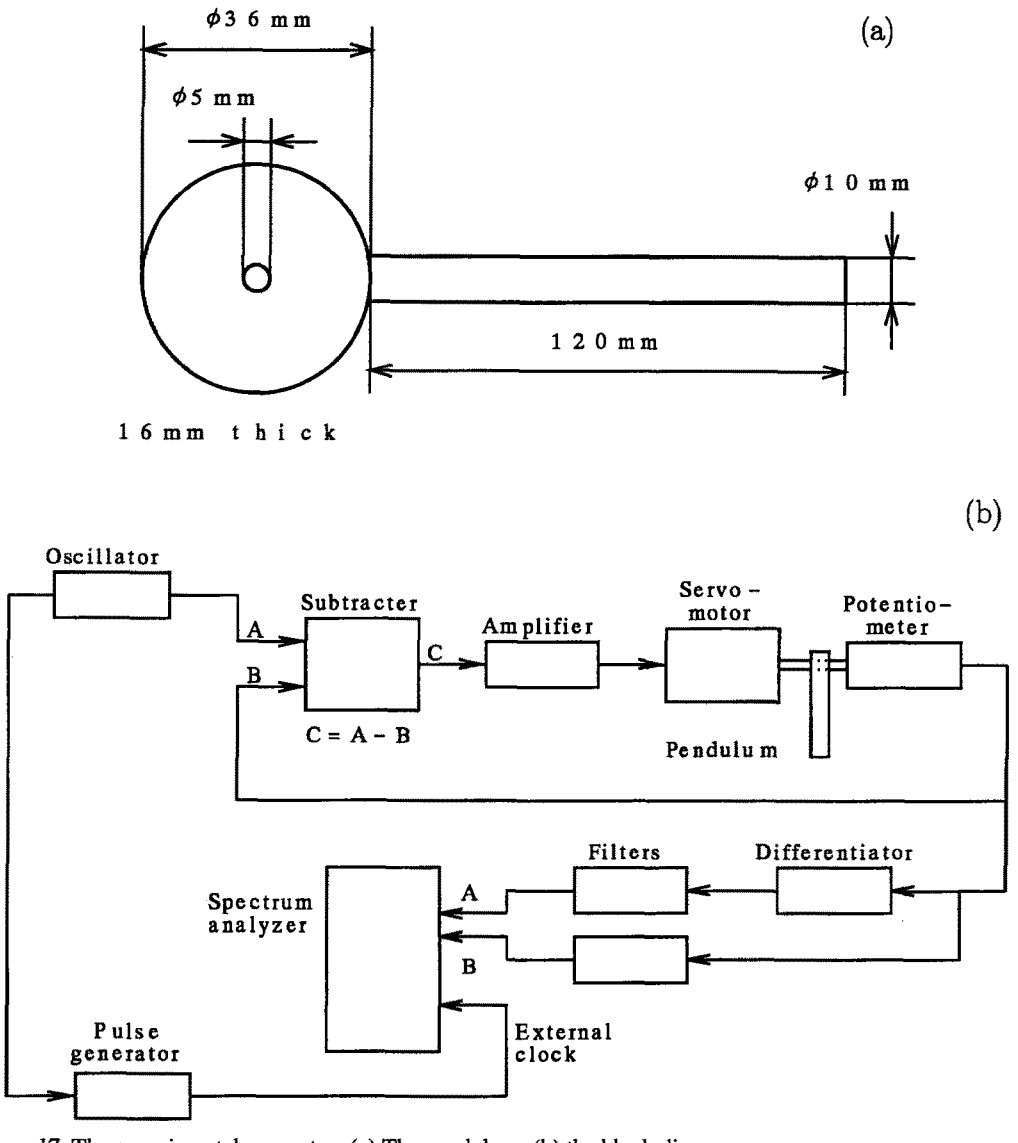

Figure 17. The experimental apparatus. (a) The pendulum; (b) the block diagram.

To estimate the damping constant, we rearranged the experimental setup so that the pendulum could rotate horizontally. In this case the nonlinear term '$\sin x$' in equation (1) must be neglected. From time histories of the pendulum for constant reference signals ($\bar{\gamma} = 0$), the damping constant $\bar{\delta} = 0.12$ was obtained. Moreover, we experimentally obtained the relation $\alpha = 0.498K$ from the damped natural frequencies (cf. equation (2)).

4.2. Experimental Results

As in Sections 2.5 and 3, the parameters α and β were fixed as follows: (i) $\alpha = 0.5$ and $\beta = 1.6$; and (ii) $\alpha = 0.15$ and $\beta = 1$. The input amplitude $\bar{\gamma}$ and the frequency ω were varied.

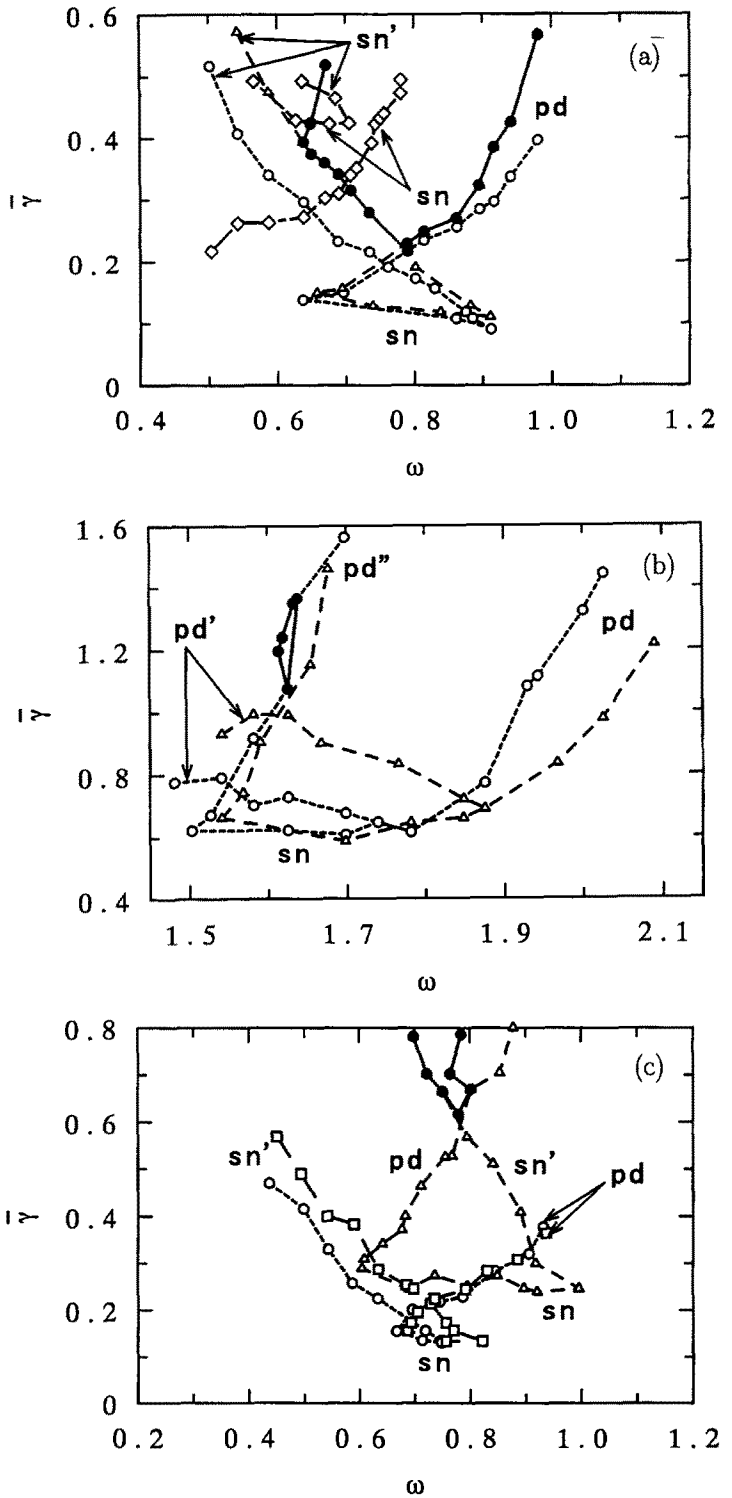

Figure 18. Bifurcation sets for harmonics or second-order subharmonics and regions for the existence of sustained chaos. (a) Near the primary resonance in case (i); (b) near the second-order subharmonic resonance in case (i); (c) near the primary resonance in case (ii).

Figure 18 shows experimentally obtained bifurcation sets for harmonics and second-order subharmonics and regions for the existence of sustained chaos. The experimental measurements near the primary and second-order subharmonic resonances in case (i) are shown in Figures 18(a) and (b), respectively, and the experimental measurements near the primary resonance in case (ii) are shown in Figure 18(c). Supercritical and subcritical saddle-node bifurcations of harmonics or subharmonics are denoted by *sn* and *sn'*, respectively, while supercritical and subcritical period-doubling bifurcations of harmonics denoted by *pd* and *pd'*, respectively, and supercritical period-doubling bifurcations of second-order subharmonics by *pd"*. In Figures 18(a) and (b) the bifurcation sets for harmonics or second-order subharmonics near the left and right unperturbed centers are plotted as open circles and triangles, respectively, while the bifurcation sets for large harmonics outside the unperturbed homoclinic loops are plotted as diamonds. In Figure 18(c) the bifurcation sets for harmonics or second-order subharmonics near the left, middle and right centers are plotted as open circles, triangles and squares, respectively. In the three figures the boundaries of regions for sustained chaos are plotted as solid circles. We should point out that in some parts above or inside the boundary curves for sustained chaos only stable periodic motions were observed. The experimental results are (at least qualitatively) in good agreement with the corresponding numerical simulation results of Figures 9, 11 and 12.

Experimentally obtained chaotic orbits of the Poincaré map and power spectra of the orbits with $\bar{\gamma} = 0.30$ and $\omega = 0.75$ for case (i) and $\bar{\gamma} = 0.82$ and $\omega = 0.75$ for case (ii) are shown in Figures 19 and 20, respectively. In each figures, figure (a) shows an orbit of the Poincaré map and figure (b) an averaged power spectrum of the displacement for 8 samples of duration 160(s), each containing 2048 data points. These experimental results are in excellent agreement with the corresponding numerical simulation results of Figures 8 and 14.

5. Conclusions

In this paper we have studied theoretically and experimentally the nonlinear dynamics of a pendulum subjected to linear feedback control with periodic desired motions. Saddle-node bifurcations of harmonics and second-order subharmonics and period-doubling bifurcations of harmonics were detected using the second-order averaging method and Melnikov's method. The Melnikov analysis was performed by numerically computing the Melnikov functions. Numerical simulations and experimental measurements were also given and compared with the theoretical predictions. Other bifurcations were found besides theoretically predicted ones. Sustained chaotic motions resulting from homoclinic and heteroclinic tangles for not only single but also multiple saddle-type periodic orbits were observed. Fairly good agreement was also found between numerical simulation and experimental results.

Some experiments have been performed for periodically forced beams to experimentally confirm the occurrence of chaos in periodically forced single-degree-of-freedom mechanical systems (e.g., [5, 15–19]). However, it was difficult in these experiments to study chaotic motions in the pure single-mode dynamics because of vibrations of higher modes (cf., [19]). In some cases the effect of higher modes may be considerable, and this seems to be true in the experiment of Li and Moon [5]. Our experimental model is good for illustrating chaotic dynamics of single-degree-of-freedom systems since there is little effect of other modes and chaotic motions are bounded, while pendulums without position feedback can rotate unboundedly. We can also experimentally observe in this model chaotic motions resulting from very complicated homoclinic and heteroclinic tangles.

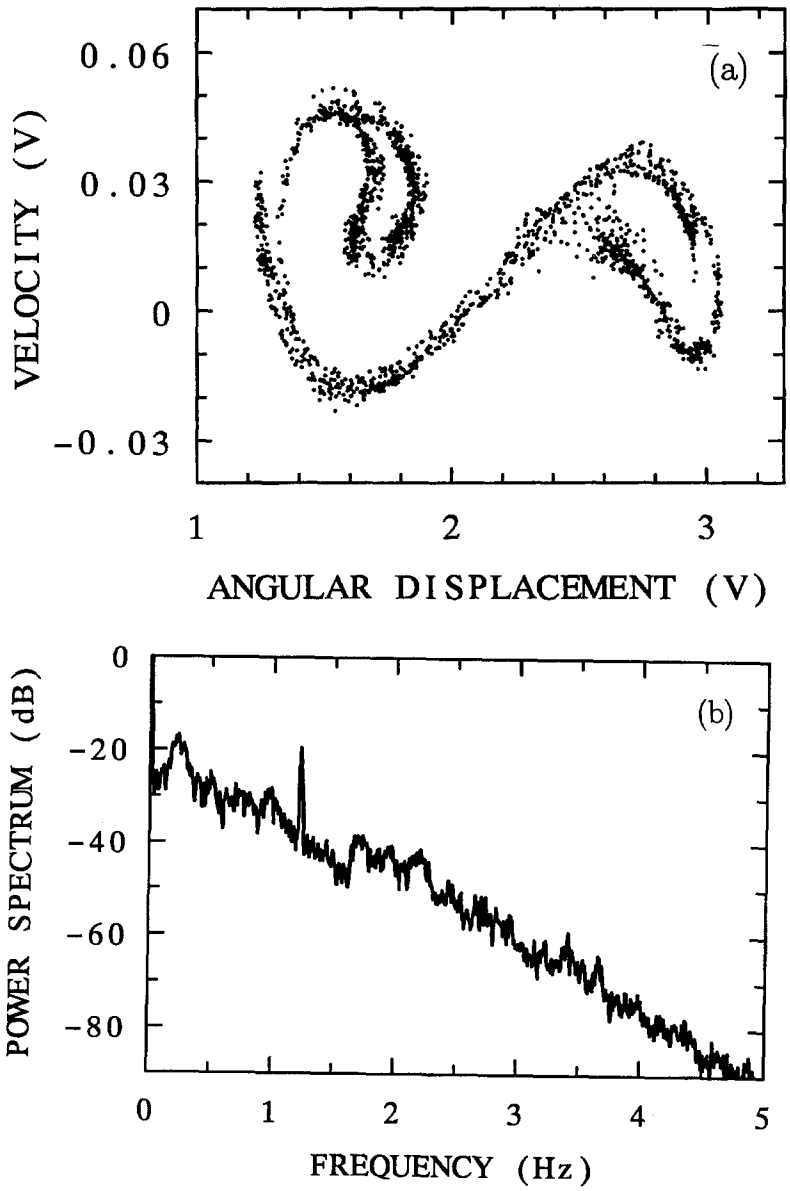

Figure 19. A chaotic motion for $\bar{\gamma} = 0.30$ and $\omega = 0.75$ in case (i). (a) An orbit of the Poincaré map; (b) a power spectrum of the angular displacement.

Our second-averaging analysis predicted that bifurcation structures near the primary and second-order subharmonic resonances in the pendulum with feedback control are similar to those in other forced nonlinear oscillators, for example, the Duffing oscillator with double well potential. The numerical simulations and experimental measurements given here also support this prediction. We may become inclined to say that there exist common structures of bifurcations near the primary, subharmonic and superharmonic resonances in a large class of forced nonlinear oscillators. Further work on this conjecture will be reported.

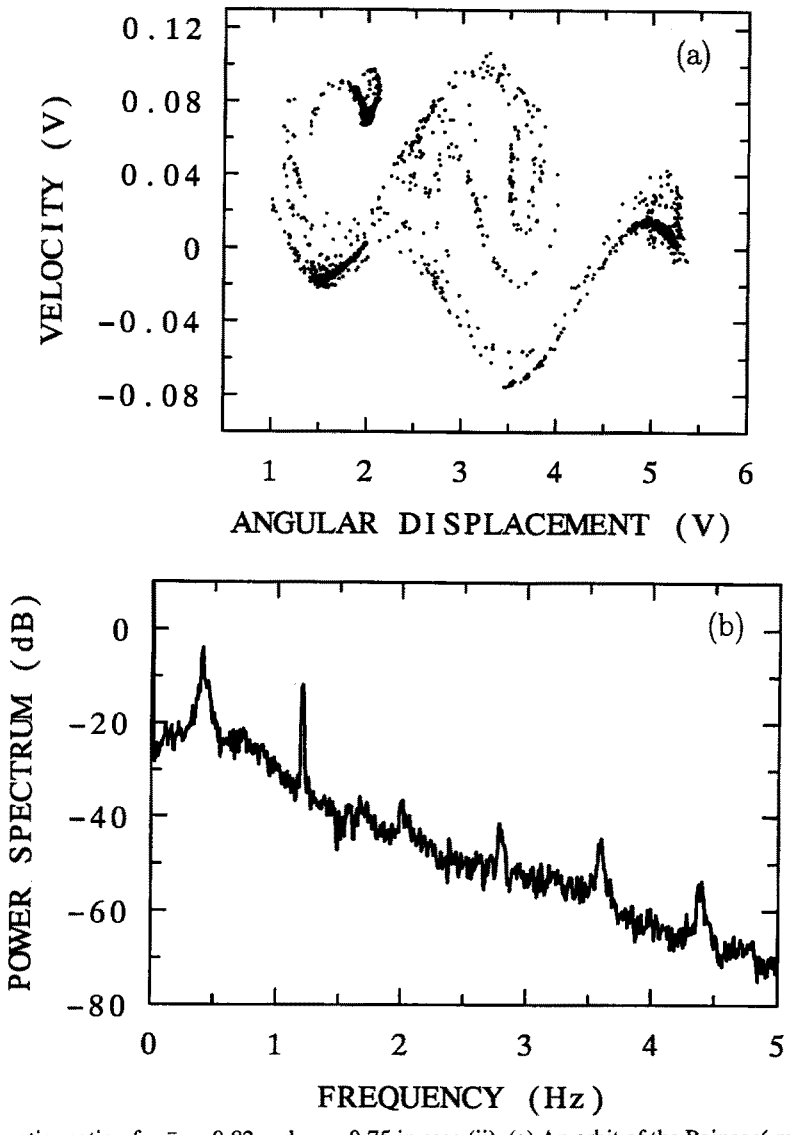

Figure 20. A chaotic motion for $\bar{\gamma} = 0.82$ and $\omega = 0.75$ in case (ii). (a) An orbit of the Poincaré map; (b) a power spectrum of the angular displacement.

Acknowledgements

This research was partially supported by a grant from the Science Foundation of the Ministry of Education of Japan, 04750210. The author thanks Takayuki Nakajima and Tadahiro Yamamoto for assistance to numerical and experimental work. He also acknowledges Naoto Yanagihara and Yoshio Hamamatsu for helpful suggestions, and Hisao Taguchi, Juichi Yasuike and Haruo Okabe for technical assistance in experiments.

References

1. Yagasaki, K., 'Chaos in a pendulum with feedback control', *Nonlinear Dynamics* **6**, 1994, 125–142.
2. Guckenheimer, J. and Holmes, P., *Nonlinear Oscillations, Dynamical Systems, and Bifurcations of Vector Fields*, Springer-Verlag, New York, 1983.
3. Wiggins, S., *Introduction to Applied Nonlinear Dynamical Systems and Chaos*, Springer-Verlag, New York, 1990.

4. Yagasaki, K., 'Second-order averaging and Melnikov analyses for forced nonlinear oscillators', *Journal of Sound and Vibration*, to appear.
5. Li, G. X. and Moon, F. C., 'Criteria for chaos of a three-well potential oscillator with homoclinic and heteroclinic orbits', *Journal of Sound and Vibration* **136**, 1990, 17–34.
6. Bruhn, B. and Koch, B. P., 'Homoclinic and heteroclinic bifurcations in rf SQUIDs', *Zeitschrift fur Naturforschung* **43a**, 1988, 930–938.
7. Gill, S., 'A process for the step-by-step integration of differential equations in an automatic digital computing machine', *Proceedings of the Cambridge Philosophical Society* **47**, 1951, 96–108.
8. Thompson, J. M. T., 'Chaotic phenomena triggering the escape from a potential well', *Proceedings of the Royal Society of London, Series A* **421**, 1989, 195–225.
9. Szemplinska-Stupnicka, W., 'The approximate analytical methods in the study of transition to chaotic motion in nonlinear oscillators', in *Engineering Applications of Dynamics of Chaos*, W. Szemplinska-Stupnicka and H. Troger (eds.), Springer-Verlag, Wien, 1991, pp. 225–277.
10. Szemplinska-Stupnicka, W., 'Cross-well chaos and escape phenomena in driven oscillators', *Nonlinear Dynamics* **3**, 1992, 225–243.
11. Szemplinska-Stupnicka, W. and Rudowski, J., 'Bifurcations phenomena in a nonlinear oscillator: approximate analytical studies versus computer simulation results', *Physica D* **66**, 1993, 363–380.
12. Janicki, K. and Szemplinska-Stupnicka, W., 'Stability of subharmonics and escape phenomena in the twin-well potential Duffing system', Institute of Fundamental Technological Research, preprint.
13. Moon, F. C., *Chaotic and Fractal Dynamics*, Wiley, New York, 1992.
14. Nusse, H. E., and Yorke, J. A., *Dynamics: Numerical Explorations*, Springer-Verlag, New York, 1994.
15. Moon, F. C. and Holmes, P. J., 'A magnetoelastic strange attractor', *Journal of Sound and Vibration* **65**, 1979, 275–296.
16. Moon, F. C., 'Experiments on chaotic motions of a forced nonlinear oscillator: strange attractors', *Transactions of the ASME. Series E. Journal of Applied Mechanics* **47**, 1980, 638–644.
17. Moon, F. C. and Shaw, S. W., 'Chaotic vibrations of a beam with non-linear boundary conditions', *International Journal of Non-Linear Mechanics* **18**, 1983, 465–477.
18. Shaw, S. W., 'Forced vibrations of a beam with one-sided amplitude constraint: theory and experiment', *Journal of Sound and Vibration* **99**, 1985, 199–212.
19. Brunsden, V., Cortell, J., and Holmes, P. J., 'Power spectra of chaotic vibrations of a buckled beam', *Journal of Sound and Vibration* **130**, 1989, 1–25.